CFD and Experimental Investigation of Desulfurization of Rejected Electrolytic Manganese Metal in Electroslag Remelting Process

QIANG WANG, RU LU, ZHIYUAN CHEN, GUANGQIANG LI, and YONGXIANG YANG

An innovative electroslag remelting furnace with a water-cooled electrode was introduced to recycle the rejected electrolytic manganese metal (EMM) scrap. To clarify the desulfurization process in the rejected EMM scrap, a transient three-dimensional comprehensive numerical model was elaborated. Using the magnetic potential vector approach, the respective electromagnetic fields were calculated *via* the Maxwell equations. The Lorentz force and the Joule heating fields were derived as phase distribution functions and interrelated *via* the momentum and energy conservation equations as source terms, respectively. The molten manganese metal droplet motion, as well as the fluctuation of the slag–metal interface, was described by the volume-of-fluid (VOF) approach. Besides, the solidification was modeled *via* the enthalpy-based technique. A thermodynamic module was established to estimate the sulfur mass transfer rate between the molten manganese metal and the molten slag. Furthermore, a factor related to the magnitude and frequency of the alternating current and the physical properties of the melt was introduced to include the electro-emulsification phenomenon. An experiment has been carried out with a commercial-scale ESR device. The predicted values of the slag temperature and sulfur content in the final manganese ingot were found to agree reasonably with the corresponding measured data. Under continuous melting of the rejected EMM scrap, molten manganese metal droplets are formed at the domain inlet, grow, and fall down. Highly conductive molten manganese metal droplets significantly change distributions of the current streamline, the Joule heating, and the Lorentz force around and within it. Moreover, droplets are inclined to rotate and move inside the mold. With the renewal of the slag–manganese interface, sulfur in the molten manganese metal is constantly transferred to the molten slag. With the applied current ranging from 3000 to 4000 A, the average sulfur content of the manganese ingot dropped from 0.0447 to 0.0291 pct, and thus, the desulfurization rate rose from 55.3 to 70.9 pct.

QIANG WANG and YONGXIANG YANG are with The State Key Laboratory of Refractories and Metallurgy, Wuhan University of Science and Technology, Wuhan, 430081 Hubei, China, and with the Key Laboratory for Ferrous Metallurgy and Resources Utilization of Ministry of Education, Wuhan University of Science and Technology, Wuhan, 430081 Hubei, China and also with the Department of Materials Science and Engineering, Delft University of Technology, 2628 CD, Delft, The Netherlands. RU LU and GUANGQIANG LI are with The State Key Laboratory of Refractories and Metallurgy, Wuhan University of Science and Technology and also with the Key Laboratory for Ferrous Metallurgy and Resources Utilization of Ministry of Education, Wuhan University of Science and Technology. Contact e-mail: liguangqiang@wust.edu.cn ZHIYUAN CHEN is with the Department of Materials Science and Engineering, Delft University of Technology.

I. INTRODUCTION

MANGANESE metal (MM) is widely used in steelmaking industry. During the smelting process, approx. 90 pct of the total manganese is consumed as deoxidizing/desulfurizing agents and alloying constituents, which improve the hardness, stiffness, and strength of steel product. In recent years, an increase in the demand for MM is promoted the global steel production growth, mainly in China.[1]

High-purity MM is commonly produced *via* hydrometallurgical and electrolytic processes. In order to transform the MM into a brittle α-phase from a ductile γ-phase at a reasonable electric current efficiency, sulfur dioxide is used as an additive to the catholyte during the electrolytic process. The usage of the sulfur dioxide, however, induces a serious increase of the sulfur

content in the produced electrolytic MM.[2,3] Due to the excessive sulfur content, it is impossible to use the rejected EMM scrap, as shown in Figure 1, in the steel manufacturing process. As a consequence, enormous manganese resources are wasted, while the rejected EMM scrap storage is hazardous in terms of soil and water contamination.

For effective recycling of the rejected EMM scrap, the electroslag refining (ESR) approach, which provided a very effective desulfurization, was successfully introduced.[4] Figure 2 depicts the schematic of the ESR furnace used for EMM scrap refining. Noteworthy is that the ESR furnace is made of copper, which diminishes the pollution risks for the refractory lining with the refined MM. In this process, an alternating current is passed from the water-cooled electrode to the water-cooled baseplate, which generates the Joule heat in the highly resistive molten slag.[5] With a vibrating feeder, the rejected EMM scrap is continuously poured into the water-cooled mold from its top outer edge. The scrap would be melted in a very short time after it enters the hot molten slag layer.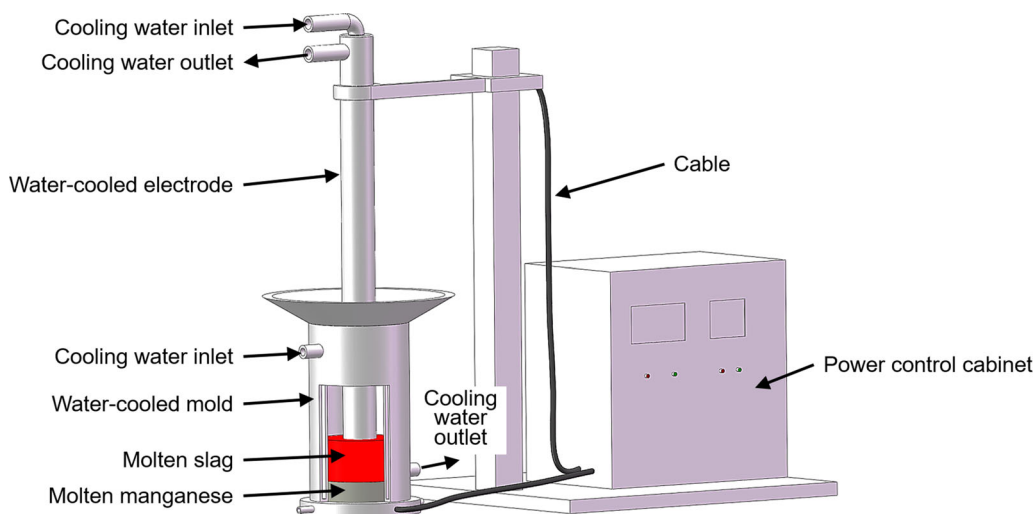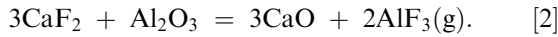 A dense manganese droplet then sinks through the molten slag layer, creating a liquid metal pool at the mold bottom. The sulfur that was dissolved in the molten manganese would be transferred to the molten slag during the refining process.[6]

Many researchers have studied the mass transfer of sulfur between the molten metal and the molten slag.[7–10] In particular, Schrama et al. investigated the sulfur removal in the ironmaking and oxygen steelmaking process[11] and reduced it to the following chemical reaction for arbitrary desulfurization conditions:

$$[S] + (O^{2-}) = (S^{2-}) + [O], \qquad [1]$$
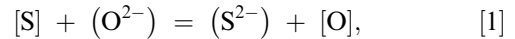
where square and round brackets indicate that the respective element is dissolved in the metal or slag, respectively. The sulfur removal is based on the following principle: the dissolved sulfur moves from the metal to the slag, and then the slag is separated from the metal. Furthermore, authors[1] assumed that higher reaction temperatures and flow velocities would lead to a more efficient desulfurization. Alba et al. experimentally studied the desulfurization of molten steel droplets passing through a molten slag layer.[12] Their results indicated that the mass transfer rate of sulfur during the dynamic contact, which occurred during the molten metal droplet fall, exceeded that of the static contact by several orders of magnitude. The continuous contact of fresh molten slag and the enhanced internal circulation within the molten metal droplets were also reported to enhance the mass transfer.

In the ESR process, the same desulfurization reaction occurs at the slag–metal interface. Sulfur in the metal would capture two electrons, provided by the oxygen ion in the slag, and enter into the slag as a sulfur ion, which would be oxidized by the oxygen in the gas atmosphere.[13,14] The oxygen ion in the slag could be generated during the process by the following reaction between CaF_2 and Al_2O_3[15]:

Fig. 1—Rejected EMM scrap.

Fig. 2—ESR furnace with water-cooled electrode for the recycling of rejected EMM scrap.

$$3CaF_2 + Al_2O_3 = 3CaO + 2AlF_3(g). \qquad [2]$$

It can be inferred that a higher CaO content would improve the sulfur removal ability of the slag. Such properties of the slag as viscosity and electrical conductivity would subsequently change. The power supply and the feeding rate of the ESR process should be adjusted accordingly.

For the theoretical substantiation of the desulfurization rate improvement of the rejected EMM scrap, it is expedient to investigate the electromagnetic field, two-phase flow, heat transfer, and solidification during the ESR process. However, the multi-factor coupled electromagnetic field arising under high-temperature and strong current conditions is hard to measure and comprehensively estimate. Alternatively, with the rapid development of numerical techniques and computing power growth, the computational fluid dynamics (CFD) approach became a powerful tool for simulating complex transport phenomena during various industrial processes.[16,17]

In the present work, a transient three-dimensional comprehensive numerical model was elaborated to simulate the electromagnetic processes, two-phase flow, thermal behavior, sulfur mass transfer, as well as solidification in the proposed process, which involved recycling of the rejected EMM scrap in the developed ESR furnace with a water-cooled electrode. The desulfurization rate was derived by means of a thermodynamic module, and variation of the sulfur content within the molten MM was clarified in detail. The developed numerical model was also experimentally validated using the ESR furnace designed by the authors. The molten slag temperature was measured via the disposable W3Re/W25Re thermocouple. The sulfur content in the remelted MM ingot was measured using a carbon and sulfur analyzer.

II. MATHEMATICAL MODEL

A. Assumptions

Given the complicated phenomena involved in the recycling process, the following assumptions are made to simplify the model:

(a) The computational domain and simulated ESR device, as shown in Figure 3, include the molten slag and molten MM, while the air space above the molten slag is ignored. The immersion depth of the water-cooled electrode in the molten slag is neglected.
(b) The two liquid phases (molten slag and MM0) are incompressible Newtonian fluids, densities of which are defined via the Bussinesq approximation. The electrical conductivity of the molten slag is temperature-dependent, while other properties of the molten slag and molten manganese are assumed to be constant.[18,19]
(c) The coefficient of the interfacial tension between the molten slag and molten MM is kept constant.[19]
(d) The molten slag and molten MM are supposed to be electrically insulated from the mold.[20]
(e) The melting of the solid rejected EMM scrap is not taken into account.
(f) The final stage of the ESR process is excluded from calculations. The applied current remains unchanged in the simulation.
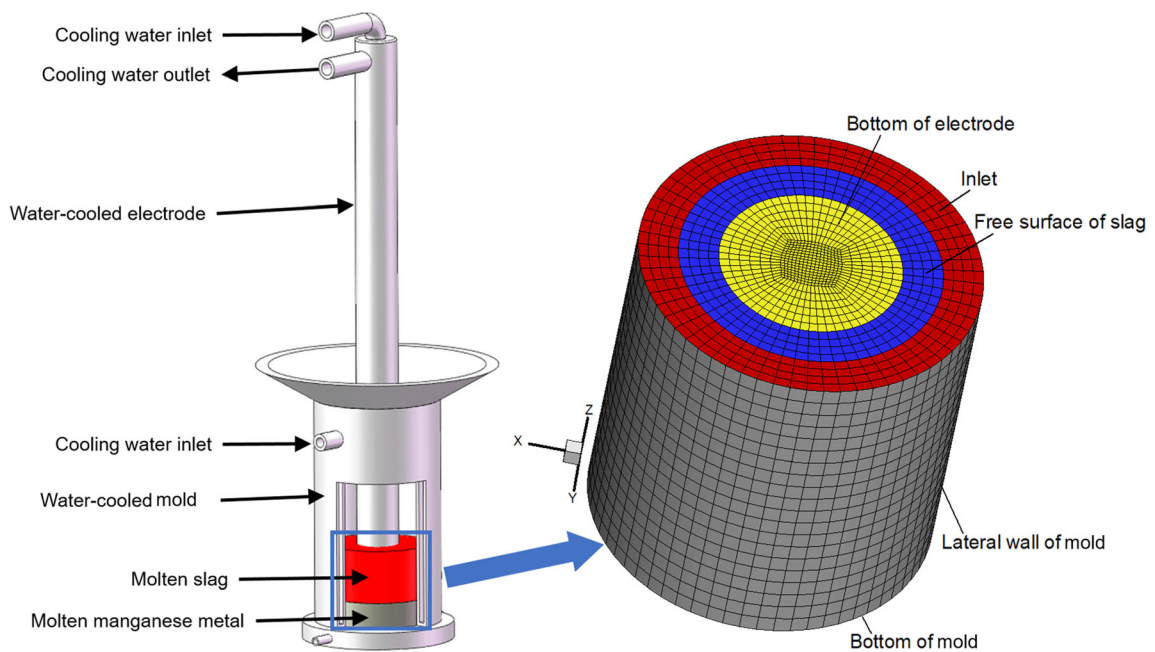(g) No other elements in the molten slag and MM, except sulfur, are analyzed.

Fig. 3—Relationship between the computational domain and the simulated ESR furnace.

(h) The chemical reaction at the slag–metal interface is considered to be quite rapid, which implies no rate-limiting step for the desulfurization.[21]

B. VOF Method

For modeling the two-phase flow of the molten slag and molten MM, the VOF method was adopted to track a scalar field variable α, namely volume fraction, within the whole domain[22,23]:

$$\frac{\partial \alpha}{\partial t} + \nabla \cdot (\vec{v}\alpha) = 0, \qquad [3]$$

where α is the volume fraction of the molten MM, t is time, and $\vec{v}$ is the motion velocity. Such properties of the mixture phase, as electrical conductivity, density, and viscosity, as related to the volume fraction as follows:

$$\bar{\phi} = \phi_m \alpha + \phi_s (1 - \alpha), \qquad [4]$$

where $\bar{\phi}$, ϕ_m, and ϕ_s are the respective properties of mixture phase, molten MM, and molten slag. The interfacial tension force between the molten slag and molten MM is described by the continuum surface force model.[24]

C. Electromagnetism

The Maxwell equations were employed to describe electromagnetic fields induced by the alternating current[5,25,26]:

$$\nabla \times \vec{H} = \vec{J} + \frac{\partial \vec{D}}{\partial t} \qquad [5]$$

$$\nabla \times \vec{E} = \nabla \times (-\nabla \varphi) = -\frac{\partial \vec{B}}{\partial t} \qquad [6]$$

$$\nabla \cdot \vec{B} = 0, \qquad [7]$$

where $\vec{H}$ is magnetic field intensity, $\vec{J}$ is current density, $\vec{D}$ is electric flux density, $\vec{E}$ is electric field intensity, and $\vec{B}$ is magnetic flux density. The current displacement $\partial \vec{D}/\partial t$ was assumed to be much lower than the electrical conduction $\vec{J}$ and could be neglected if the electrical conductivity was not too small. The constitutive equations for the electromagnetic fields have the following form:

$$\vec{B} = \bar{\mu}_0 \vec{H} \qquad [8]$$

$$\vec{J} = \bar{\sigma}\left(\vec{E} + \vec{v} \times \vec{B}\right) = \bar{\sigma}\left[(-\nabla \varphi) + \vec{v} \times \vec{B}\right], \qquad [9]$$

where $\bar{\mu}_0$ and $\bar{\sigma}$ are vacuum permeability and electrical conductivity of the mixture phase, respectively. According to the previous study, the magnetic Reynolds number, which expresses the ratio of the magnetic convection to magnetic diffusion, is very low during the ESR process.[24] As a result, Eq. [9] can be reduced to

$$\vec{J} = \bar{\sigma}\vec{E} = \bar{\sigma}(-\nabla \varphi). \qquad [10]$$

To solve the above governing equations, a well-known electrical potential approach, which implies a simultaneous derivation of the electrical potential φ and magnetic potential vector $\vec{A}$, was utilized. The electrical potential equation was deduced from the electrical current balance equation as follows:

$$\nabla \cdot \vec{J} = 0 \text{ with } \vec{J} = -\bar{\sigma}\frac{\partial \vec{A}}{\partial t} - \bar{\sigma}\nabla \varphi. \qquad [11]$$

At the same time, the magnetic potential vector was related to the magnetic field by

$$\vec{B} = \nabla \times \vec{A}. \qquad [12]$$

Harmonic electromagnetic fields can be decomposed into a time-dependent and steady component. Numerical studies on electromagnetically driven flow proved that the alternating current period, which controlled the variation period of the electromagnetic fields, was much shorter than the momentum response time of the liquid metal if its frequency exceeded 5 Hz.[19,27,28] The time-averaged Lorentz force and Joule heating were derived as follows:

$$\vec{F}_L = \vec{J} \times \vec{B} \quad \text{and} \quad Q_J = \frac{\vec{J} \cdot \vec{J}}{\bar{\sigma}}, \qquad [13]$$

where $\vec{F}_L$ is the Lorentz force and Q_J is the Joule heating.

D. Fluid Flow

Both continuous and time-averaged Navier–Stokes equations were invoked to describe the turbulent motion of both melts[25]:

$$\frac{\partial \bar{\rho}}{\partial t} + \nabla \cdot (\bar{\rho}\vec{v}) = 0 \qquad [14]$$

$$\frac{\partial(\bar{\rho}\vec{v})}{\partial t} + \bar{\rho}\,\vec{v}\nabla \cdot \vec{v} = -\nabla p + \nabla \cdot \left[\bar{\mu}\left(\nabla\vec{v} + \nabla\vec{v}^{\mathrm{T}}\right)\right] + \vec{F}_{\mathrm{ST}} + \vec{F}_{\mathrm{L}} + \vec{F}_{\mathrm{T}} + \vec{F}_{\mathrm{D}}, \qquad [15]$$

where $\bar{\rho}$ is the mixture phase density, p is pressure, $\bar{\mu}$ is the dynamic viscosity of the mixture phase. $\vec{F}_{\mathrm{ST}}$ and $\vec{F}_{\mathrm{L}}$ are the interfacial tension and the Lorentz force, respectively. $\vec{F}_{\mathrm{T}}$ is the thermal buoyancy force determined by the Boussinesq approximation, and $\vec{F}_{\mathrm{D}}$ is the damping force in the mushy zone, which is used to denote the resistance induced by the solidification. Here, the enthalpy-porosity technique was employed to model the mushy zone and solidified metal. The mushy zone was treated as a quasi-porous medium, and the porosity gradually dropped from 1 to 0 as the molten metal solidified.[29] In the fully solidified metal, the porosity was assumed to be equal to zero, thus extinguishing the velocity in this region. The damping force can be written as

$$\vec{F}_{\mathrm{D}} = \frac{(1 - f_{\mathrm{l}})}{f_{\mathrm{l}}}\,A_{\mathrm{mush}}(\vec{v} - \vec{v}_{\mathrm{cast}}) \qquad [16]$$

$$f_{\mathrm{l}} = \frac{T - T_{\mathrm{s}}}{T_{\mathrm{l}} - T_{\mathrm{s}}}, \qquad [17]$$

where f_{l} is the liquid fraction; A_{mush} is the mushy zone resistance constant; T, T_{s}, and T_{l} are current, solidus, and liquidus temperatures, respectively; $\vec{v}_{\mathrm{cast}}$ is the solidified metal flow/motion speed. In the ESR process, the solidification front moves upward slowly, since the melt rate is very low. The motion speed in Eq. [16] is therefore ignored. Additionally, the realizable k-ε turbulence model was utilized to predict the mean flow characteristics of the turbulent flow within the mold. An enhanced wall function was incorporated into the realizable k-ε turbulence model, in order to modify the fully turbulent law, so that it would take into account other effects such as pressure and temperature gradients. This formula also guarantees a reasonable representation of velocity profiles in cases they fall within the wall buffer region.

E. Heat Transfer and Solidification

The energy equation used for the solidification process is as in Reference 30

$$\frac{\partial}{\partial t}(\bar{\rho}H) + \nabla \cdot (\bar{\rho}\vec{v}H) = \nabla \cdot (k_{\mathrm{T}}\nabla T) + \xi \cdot Q_{\mathrm{J}}, \qquad [18]$$

where k_{T} is the effective thermal conductivity. It is derived as a sum of the thermal k_{t} and turbulent k_{tt} thermal conductivities. For the realizable k-ε turbulence model, we get

$$k_{\mathrm{tt}} = \frac{c_{\mathrm{p}}\mu_{\mathrm{t}}}{\mathrm{Pr}_{\mathrm{t}}} \text{ and } \mu_{\mathrm{t}} = \bar{\rho}C_{\mu}\frac{k^2}{\varepsilon}, \qquad [19]$$

where c_{p} is the specific heat at constant pressure, μ_{t} is turbulent viscosity, Pr_{t} is the turbulent Prandtl number, C_{μ} is the turbulence model parameter, k and ε are turbulence kinetic energy and dissipation rate, respectively. Noteworthy is that ξ in Eq. [18] is power efficiency, i.e., the Joule heating used to maintain the temperature of the melt. An accurate estimate of power efficiency is quite problematic, insofar as it varies under different operation conditions. Using literary data that complied with our experimental conditions,[4,5,19] the power efficiency value of 0.6 was assumed in this study. Besides, H denotes the slag and MM enthalpy, which is composed of the sensible enthalpy, h, and the latent heat ΔH:

$$H = h + \Delta H \qquad [20]$$

$$h = h_{\mathrm{ref}} + \int_{T_{\mathrm{ref}}}^{T} c_{\mathrm{p}}\mathrm{d}T \qquad [21]$$

$$\Delta H = f_{\mathrm{l}} \cdot L, \qquad [22]$$

where h_{ref} is the reference enthalpy, T_{ref} is the reference temperature, and L is the latent heat.

F. Mass Transfer of Sulfur

Sulfur in the molten MM would be transferred to the molten slag because of the permanent contact reaction at the slag–metal interface. The two film theory was applied to analysis the mass transfer of sulfur between the molten slag and the molten MM. As mentioned above, the chemical reaction was fast enough and therefore not being the rate-limiting step. The potential rate-limiting step for the desulfurization was supposed to be the mass transport of sulfur within the melt. The difference of the sulfur concentration at each side of the slag–metal interface was regarded as the driving force in the desulfurization kinetics, while the convection and the diffusion of sulfur within the molten slag and the molten MM significantly affected the desulfurization. These phenomena can be described as in References 31 and 32

$$\frac{\partial(\bar{\rho}c)}{\partial t} + \nabla \cdot (\bar{\rho}\vec{v}c) = \nabla \cdot (\zeta \cdot \bar{D}_s \nabla c), \qquad [23]$$

where c is concentration of sulfur shared by the two phases, and $\bar{D}_s$ is diffusion coefficient of sulfur of the mixture phase, which is related to the individual diffusivity of each phase.[33–35] Besides, it should be recognized that the MM droplet would deform and oscillate during its falling process under the effect of the alternating current, which is referred to as electro-emulsification.[36,37] The reaction area for the desulfurization would be, therefore, remarkably increased by the electro-emulsification. In the present work, the factor ζ was utilized to include the effect of the electro-emulsification on the sulfur mass transfer. The factor was associated with the electric field strength $\vec{E}$, power frequency f, dynamic viscosity of each fluid μ, and the interfacial tension coefficient γ[38,39]:

$$\zeta = \frac{9\varepsilon_0\varepsilon_m\left|\vec{E}_0\right|^2 r_d}{32\gamma}\frac{1}{\sqrt{1+\bar{k}^2\lambda_2^2}}\cos(2\omega t + \psi) \qquad [24]$$

$$\bar{k} = \frac{\omega\mu_m r_d}{\gamma} \qquad [25]$$

$$\lambda_2 = \frac{(16\lambda + 19)(3\lambda + 2)}{20(\lambda + 1)} \qquad [26]$$

$$\lambda = \frac{\mu_m}{\mu_s} \qquad [27]$$

$$\omega = 2\pi f, \qquad [28]$$

where ε_0 and ε_m are permittivity values of the free space and molten MM, respectively, $\vec{E}_0$ is the electric field intensity far from the MM drop, r_d is radius of the undeformed MM droplet, μ_m and μ_s are dynamic viscosities of the molten MM and molten slag, respectively, and ψ is the initial phase angle of the alternating current.

G. Boundary Conditions

A zero potential was imposed at the bottom of the mold, while a potential gradient was applied at the bottom of the water-cooled electrode. It can be calculated that the skin effect depth for the copper with a 50 Hz power frequency is around 10 mm, which was equal to the thickness of the cooper pipe used in the water-cooled electrode. The current density at the bottom of the water-cooled electrode therefore was uniform. Besides, the free surface of the molten slag, the inlet and the lateral wall of the mold were assumed to be electrically insulated[5]:

$$\frac{\partial\varphi}{\partial\vec{n}} = 0 \qquad [29]$$

where $\vec{n}$ is the unit normal vector. The magnetic flux density was supposed to be continuous at the bottom of the electrode, free surface of the molten slag, inlet and the bottom of the mold. It was presumed to be negligibly small at the mold lateral wall[19]:

$$A_x = A_y = \frac{\partial A_z}{\partial z} = 0 \qquad [30]$$

$$A_x = A_y = A_z = 0, \qquad [31]$$

where A_x, A_y, and A_z are the magnetic potential vectors along x-, y-, and z-axes, respectively.

A mass flow rate, equaled to the addition rate of the rejected EMM scrap in the experiment, was adopted at the inlet. A no-slip wall condition was applied to the bottom of the electrode, and the lateral wall and the bottom of the mold. In order to better define the free surface flow, zero shear stress was employed on the free surface of the molten slag.

To simplify the melting process, the rejected EMM scrap was assumed to be liquid at the inlet with a constant temperature of 1537 K (1264 °C). Since the furnace was placed in the air atmosphere, the free surface of the molten slag was supposed to exchange heat with the surrounding air by both the natural convection and the thermal radiation. Equivalent heat transfer coefficients were also applied to the bottom of the electrode, and the lateral wall and the bottom of the mold to represent the heat exchange between the melt and the cooling water.

The mass fraction of sulfur at the inlet was kept at 0.1 pct, which was equivalent to that of the rejected EMM scrap used in the experiment. A zero flux was imposed at the bottom of the electrode, the free surface of the molten slag, the lateral wall and the bottom of the mold, indicating sulfur was not allowed to leave the domain. The detailed physical properties, the geometrical and operating conditions are listed in Table I.

III. SIMULATION PROCEDURE

The ANSYS-FLUENT 18.1 general-purpose commercial software was employed for the numerical simulations. The magnetic potential vector, electro-emulsification submodel, and boundary conditions for the electromagnetic module were incorporated into the original software program developed by the authors.

All governing equations of the electromagnetism, two-phase flow, heat and mass transfer, as well as solidification, were integrated over each control volume and simultaneously solved by using an iterative procedure. A standard pressure interpolation scheme was required to compute the face values of pressure from the cell values. The SIMPLE algorithm was applied in pressure-velocity coupling in the segregated solver to

Table I. Physical Properties, Geometry, and Operating Conditions

Parameter	Value
Physical Properties of the Molten Manganese	
Density (kg/m^3)	5950
Dynamic Viscosity (Pa s)	0.0036
Latent Heat of Fusion (kJ/kg)	710
Thermal Conductivity (W/m K)	7.03
Specific Heat (J/kg K)	840
Electric Conductivity (Ω^{-1}/m)	5.74×10^5
Magnetic Permeability (H/m)	1.257×10^{-6}
Thermal Coefficient of Cubical Expansion (K^{-1})	1.7×10^{-4}
Physical Properties of the Molten Slag	
Density (kg/m^3)	2800
Dynamic Viscosity (Pa·s)	0.025
Thermal Conductivity (W/m·K)	10.46
Specific Heat (J/kg K)	1255
Electric Conductivity (Ω^{-1}/m)	$\ln \sigma = -6769.0/T + 8.818$
Magnetic Permeability (H/m)	1.257×10^{-6}
Thermal Coefficient of Cubical Expansion (K^{-1})	2.1×10^{-4}
Geometry and Operating Conditions	
Outer Diameter of the Water-Cooled Electrode (m)	0.16
Inner Diameter of Mold (m)	0.3
Slag Height (m)	0.26
Feed rate of Rejected EMM Scrap (kg/s)	0.02
RMS Value of Alternating Current (A)	3000/3500/4000
Frequency (Hz)	50

adjust the velocity fields by correcting the pressure field.[40,41] The second-order upwind scheme was chosen to discretize each governing equation for a higher accuracy. Before advancing, the iterative procedure was continued until all normalized unscaled residuals were less than 10^{-6}.

Due to the continuous adding of the rejected EMM scrap, the MM layer height would grow, thus moving upward the molten slag layer. The dynamic mesh technique was adopted to include the height increment of the computational domain during the recycling process. The top row of the control volume of the computational domain was allowed to spawn a new row of the control volume when its height was increased by 25 pct. In addition, the mesh independency was thoroughly tested. Three structured grid models were created to discretize the physical domain with the respective sizes of 2, 4, and 6 mm. The velocity magnitude and temperature of the four monitoring points for the three types of the grids were examined after a typical simulation. The ensemble average deviations of the velocity magnitude and temperature of the four points for the first and second meshes were about 2.46 and 1.22 pct, while they were 9.54 and 7.88 pct between the second and the third meshes, respectively. Besides, the value of $y+$ within the grids adjacent to the wall was equal to ~1. Considering high computation cost, the second mesh was used in further computations. The grid pattern and boundary conditions can be seen in Figure 3 in Section II. It is noteworthy that the MM initial height is assumed to be 10 mm in the present work, while a liquid state of the slag and MM is assumed at the beginning of the simulation. Approximately 600 CPU hours of a 8-core 4.1 GHz PC with a 0.001 second time step were required for one typical simulation.

IV. INDUSTRIAL EXPERIMENT

A commercial-scale experiment was conducted using an ESR furnace with a water-cooled electrode in ambient air as shown in Figure 4(a). The mold inner diameter and height were 300 and 1500 mm, respectively. The water-cooled copper electrode with a 160 mm outer diameter was inserted into the molten slag.

The composition of the rejected EMM scrap, as displayed in Table II, was analyzed by an inductively coupled plasma atomic emission spectroscopy (ICP-AES) and X-ray photoelectron spectroscopy (XPS). The molten slag composition was 70 wt pct CaF$_2$ and 30 wt pct Al$_2$O$_3$. The thickness of the molten slag layer was 260 mm and remained unchanged during the recycling process.

An alternating current, with RMS of 3500 A and frequency of 50 Hz, was applied to the electrode. The solid rejected EMM scrap was continuously added to the mold with a constant rate of 0.02 kg/s. During the recycling process, the molten slag temperature was measured by a disposable W3Re/W25Re thermocouple every 15 minutes. Additionally, samples of the refined MM, as illustrated in Figure 4(b), were taken from the upper, middle, and lower parts of the final ESR ingot and their sulfur concentrations were measured using a carbon sulfur analyzer.
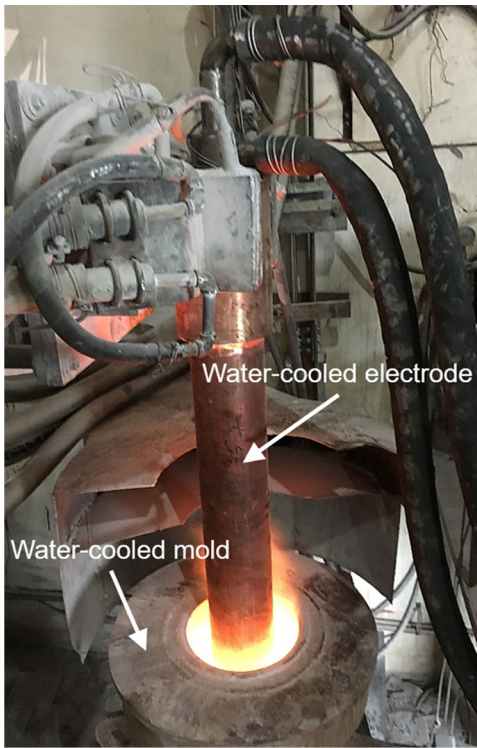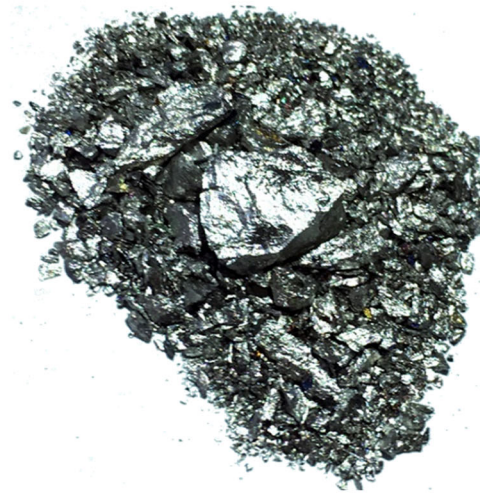
Fig. 4—Photos of the experimental set-up: (*a*) ESR furnace and (*b*) refined MM.

Table II.   Composition of the Rejected EMM Scrap, Wt Pct

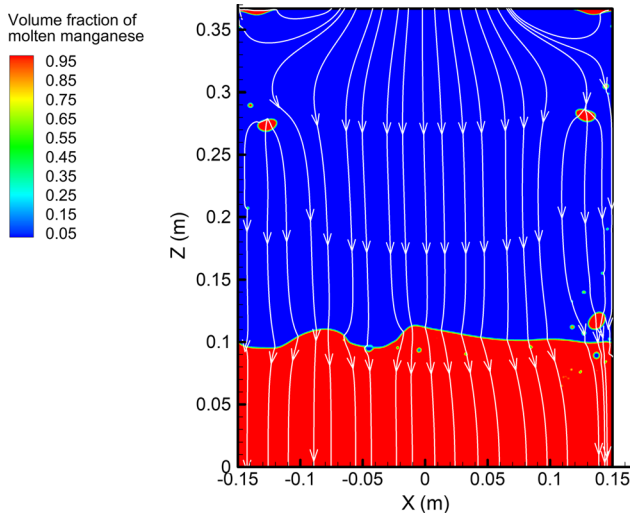| Mn	Se	C	S	P	Si	Fe	O
97.657	0.056	0.013	0.100	0.121	0.020	1.909	0.124

Fig. 5—Distributions of electrical current streamlines, molten slag and molten MM at t_0 + 0.4 s with 3500 A applied current.
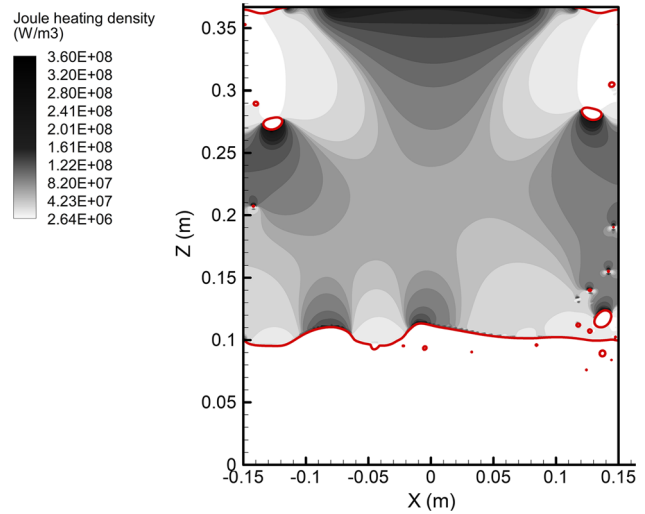

Fig. 6—Distributions of Joule heating and slag–metal interface (red line) at t_0 + 0.4 s with 3500 A applied current.

V.   RESULTS AND DISCUSSION

A. *Electromagnetic Phenomena*

Figure 5 depicts distributions of the electrical current streamlines and two phases, *i.e.*, the molten slag and molten MM. It is obvious that the electrical current streamlines are dramatically distorted at the slag–metal

interface due to the difference between the molten MM and molten slag. Since the electrical conductivity of the molten MM is about 1000 times higher than that of the molten slag, the electrical current firstly passes the molten MM droplet during its falling process, which considerably alters the Joule heating distribution (Figure 6). Most of the Joule heating is created by the molten slag because of its lower electrical conductivity, *i.e.*, higher electrical resistance, as mentioned above. Additionally, the electrical current first passes the droplet and then continuously moves downward together with the droplet within the molten slag layer. Consequently, the current density around the droplet becomes higher, contributing to the generation of the Joule heating. A higher Joule heating density is therefore observed around the droplet. A lower Joule heating density appears at the top outer edge of the mold due to the lower current density.

It is noteworthy that discontinuous current streamlines in Figure 5 are caused by the 3D effect. The electrical current enters the droplet from the upper part and then comes out from the bottom, but not in the same plane. The electrical current above the droplet seems to disappear if the electrical current streamline distribution is visualized in a vertical plane. The same discrepancy occurs for the Joule heating distribution in the vertical plane in Figure 6, since the Joule heating map is determined by the current density distribution.

A clockwise magnetic field would be induced by the downward electrical current (being observed from the mold top). The interaction between the magnetic field and electrical current gives rise to an inward Lorentz force, which phenomenon has been reported previous works of the authors.[6,42,43] Figure 7 demonstrates an enlarged view of the Lorentz force around the droplet and the slag–metal interface. It is seen that the Lorentz
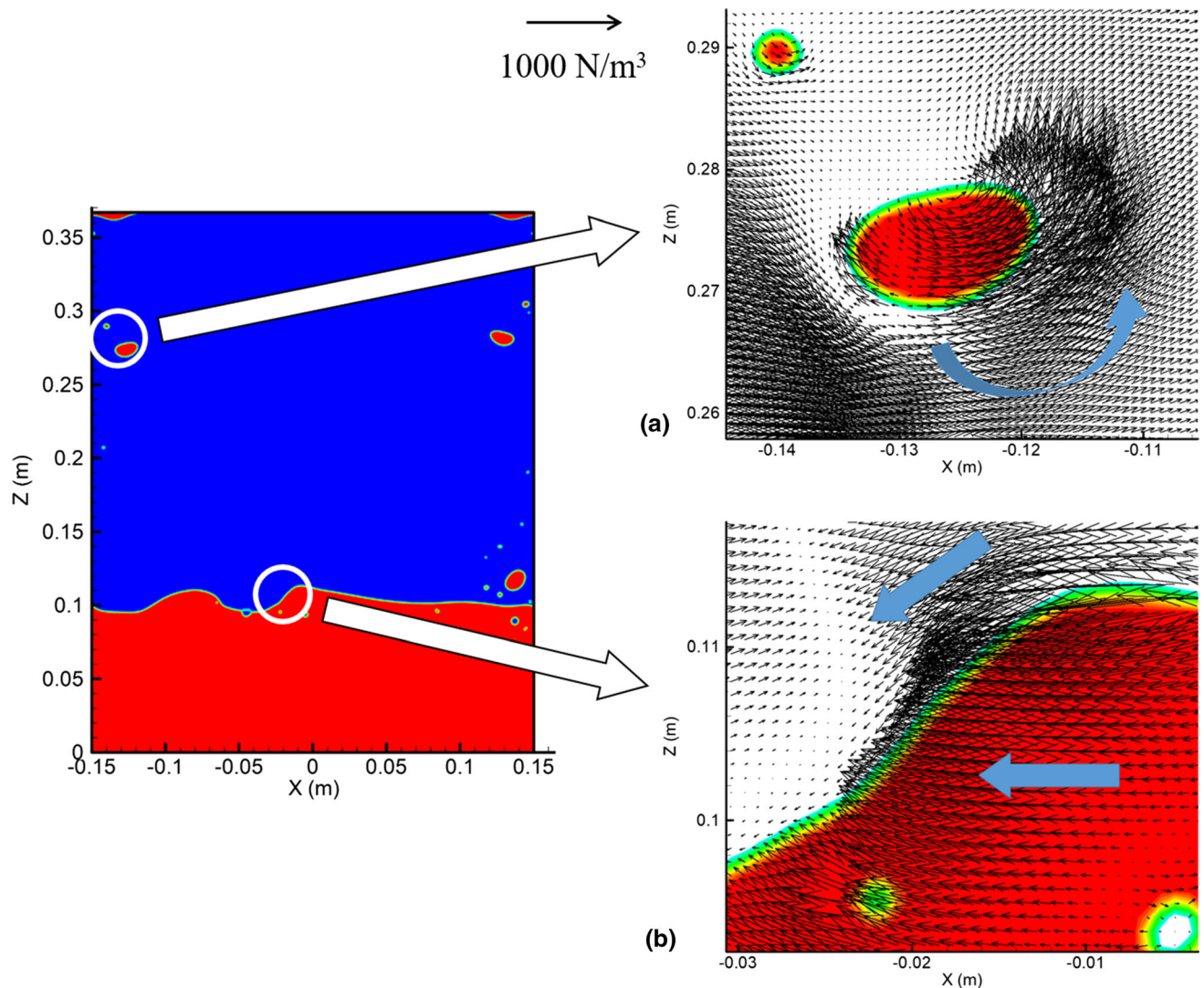

Fig. 7—Lorentz force field at $t_0 + 0.4$ s with 3500 A applied current: (*a*) Lorentz force field around droplet and (*b*) Lorentz force field around slag–metal interface.
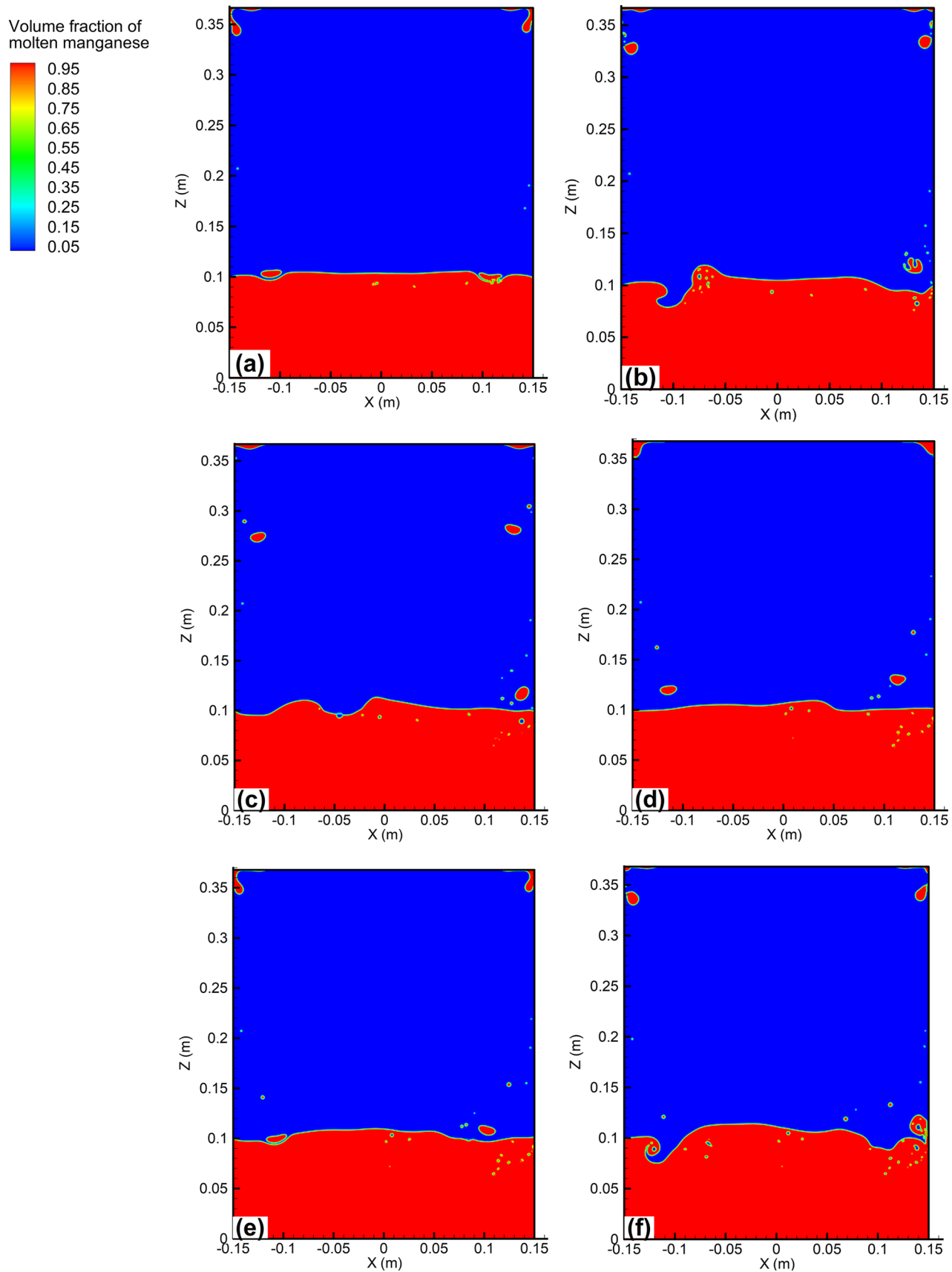
Fig. 8—Distribution of molten slag and molten manganese: (*a*) t_0 s, (*b*) $t_0 + 0.2$ s, (*c*) $t_0 + 0.4$ s, (*d*) $t_0 + 1.0$ s, (*e*) $t_0 + 1.1$ s, and (*f*) $t_0 + 1.2$ s.

force within and around the droplet rotates in the counterclockwise direction, rather than points inward, because of the distorted electrical current streamline. Under the Lorentz force action, the metal droplet would migrate inside the mold while descending. Furthermore, the twisted electrical current streamline near the slag–metal interface would generate an oblique Lorentz force, instead of a horizontal one, promoting the slag–metal interface fluctuation and the sulfur mass transfer rate.

B. Flow and Thermal Fields

Figure 8 shows the evolution of both phases with time. Since the rejected EMM scrap is dumped into the mold with a constant rate of 0.02 kg/s, molten MM droplets are regularly formed at the inlet and gradually grow during the recycling process (Figure 8(a)). These droplets would then deform and move toward the side wall of the mold under the action of the molten slag flow, as seen in Figure 9. A hotter molten slag located at the top layer first moves to the outer edge of the mold, which pushes the droplet to the lateral wall of the mold as mentioned above. And from there, the molten slag becomes denser and moves downward along the lateral wall of the mold because of the water cooling. The molten slag then turns around when approaching the slag–metal interface. A pair of vortexes is therefore created in the molten slag layer by the buoyancy force. With droplets' growth, their necks progressively taper off and, finally, droplets became separated from the domain inlet and drip down under the gravity effect, as displayed in Figure 8(b). The combined action of the Lorentz force, interfacial tension, and gravity change the shape and motion path of droplets during their descending. A dramatic fluctuation is caused by the droplet contact with the slag–metal interface, as depicted in Figure 8(f). It takes about 3.1 seconds for the droplet to enter the molten manganese pool after its formation with a 3500 A current and a 0.02 kg/s feed rate.

A shallow metal pool is formed at the mold bottom, since the heat is extracted by the cooling water at the bottom and the lateral wall. As a result, the influence of the buoyancy force lags behind that of the inward Lorentz force and the interfacial force within the metal pool, due to the heat insulation effect of the solidified metal. A counterclockwise circulation (if the right side of Figure 9 is observed) is presumed to result from the inward Lorentz force and the drag-force exerted by the molten slag layer with a higher viscosity.

Figure 10 represents distributions of the temperature and solidification front. The temperature of the molten slag at the top layer is obviously higher, although the heat of the molten slag would be taken away by the water-cooled electrode. It is mainly because the Joule heating in the slag is higher than that below the water-cooled electrode, due to a higher current density (Figure 6), and the heating effect outweighs the water cooling one. Besides, a hotter zone is observed at the bottom of the molten slag layer due to higher Joule heating and lower heat losses. A hotter region below the center of the molten slag layer is also generated by the convection.

As seen in Figure 6, the Joule heating in the molten slag is more intensive than that around the metal droplet. However, a certain period of response time is required for the increase in the molten slag temperature. As a result, an increasing in the molten slag temperature lags behind the metal droplet descending process. This can justify the absence of a high-temperature region below the metal droplet.

Since a great deal of heat is extracted by the cooling water from this region, a thin slag crust is formed and attached to the mold lateral wall and the bottom of the electrode. The average thickness of the slag crust at the bottom of the electrode is about 4 mm, according to the simulation results. In the experiment, a solidified slag layer of approx. 3 mm in thickness was observed at the bottom of the electrode, after the electrode was lifted. At the base of the mold, the molten MM gradually froze
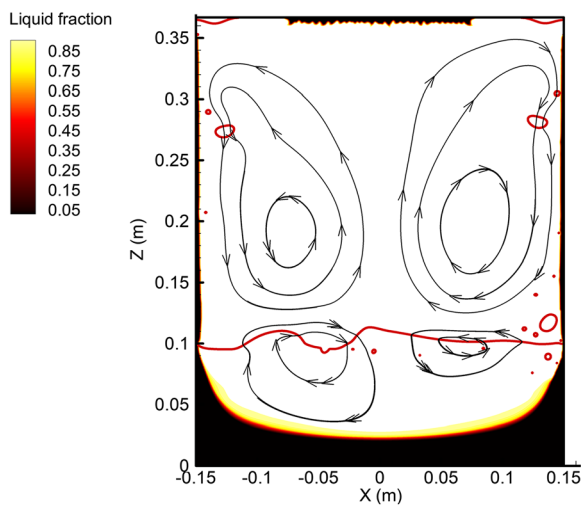

Fig. 9—Distributions of flow streamlines (black line), slag–metal interface (red line) and liquid fraction at $t_0 + 0.4$ s with 3500 A applied current (Color figure online).
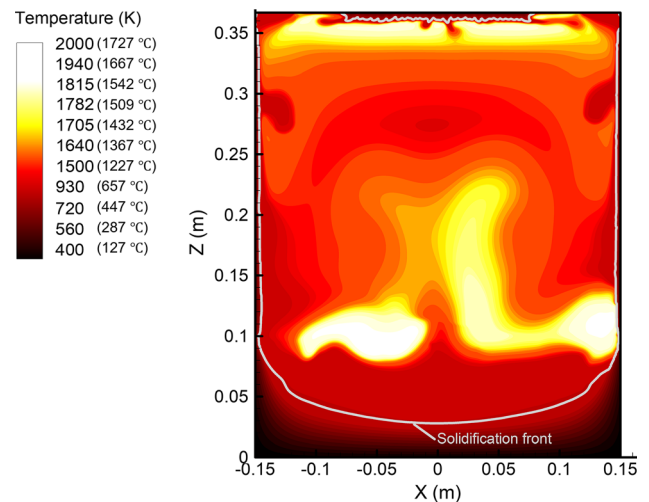

Fig. 10—Distributions of temperature and solidification front (gray line) at $t_0 + 0.4$ s with 3500 A applied current.
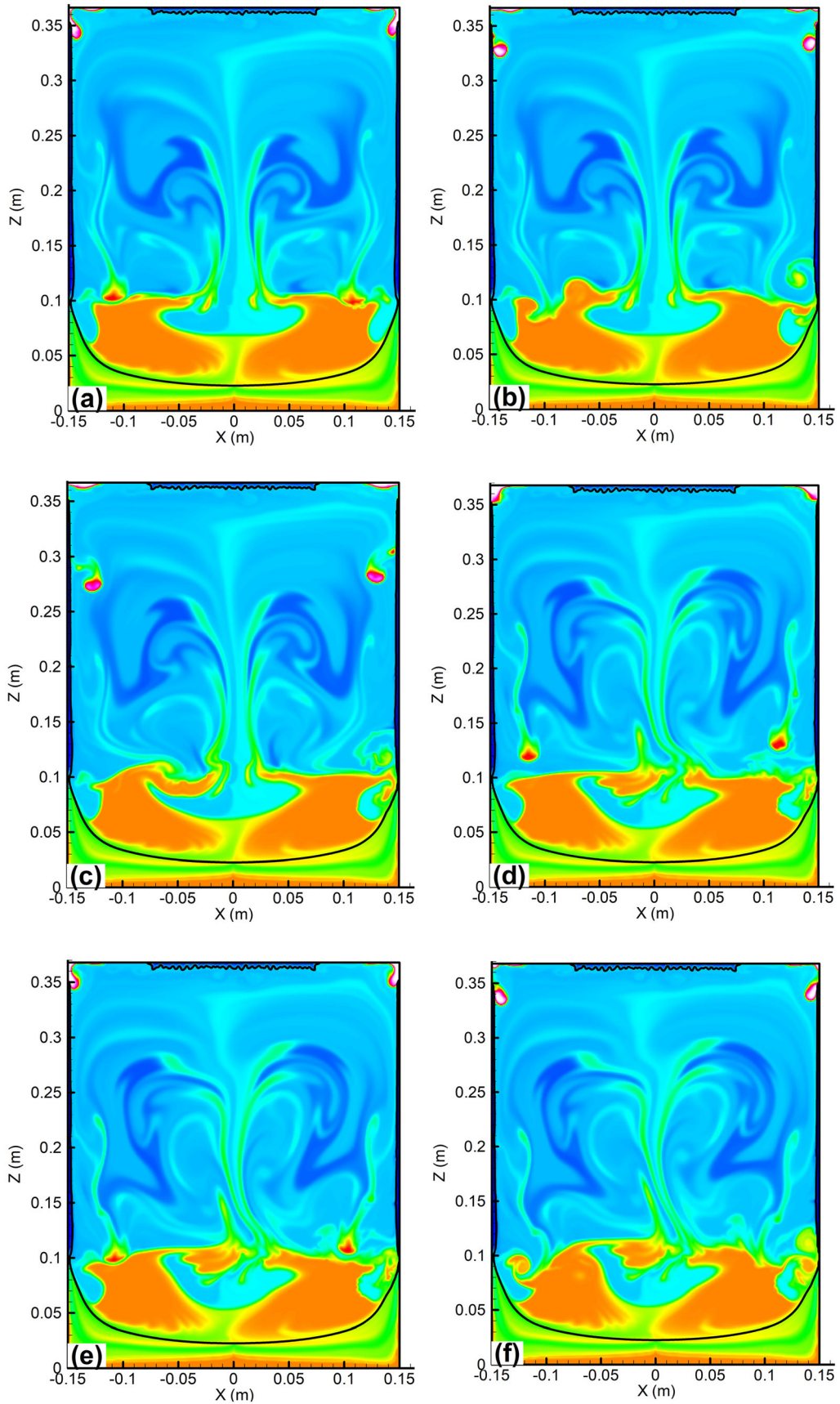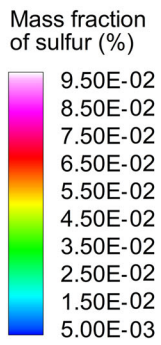
Fig. 11—Distribution of sulfur at molten slag and molten manganese: (*a*) t_0 s, (*b*) $t_0 + 0.2$ s, (*c*) $t_0 + 0.4$ s, (*d*) $t_0 + 1.0$ s, (*e*) $t_0 + 1.1$ s, and (*f*) $t_0 + 1.2$ s.

under the effect of the cooling water. At the beginning of the recycling process, a shallow flat metal pool was developed, which eventually became U-shaped. This can be attributed to the fact that the heat resistance in the vertical direction grows with the solidification of the MM, while the cooling effect of the mold bottom lags behind that of the mold lateral wall.

C. *Sulfur Mass Transfer Behavior*

Figure 11 illustrates the sulfur concentration distribution in both phases at different periods. It is known that the desulfurization reaction takes place at the slag–metal interface. From Figures 11(a) and (b), it is easy to find that the sulfur concentration of the molten MM close to the droplet surface is lower than that at the center of the droplet. The convection around and within the droplet greatly promotes the homogenization of the sulfur concentration in the droplet with the dripping process as seen in Figure 11(c). The slag–manganese interface can be also renewed, since the molten manganese inside the droplet would flow to the outside surface of the droplet, while the molten manganese at the surface layer tends to move back to the inner of the droplet. Sulfur of the molten manganese at the center of the droplet is therefore migrated to the outer layer of the droplet, and be removed by the molten slag afterwards. More opportunities are therefore provided for the desulfurization of the molten manganese.

After sulfur is transferred to the molten slag flow, its diffusion is driven by the concentration difference, while it moves with the flow. The content of sulfur in the molten slag, the downstream of the flow of the droplet, is higher than that in the other region of the molten slag, as shown in Figure 11(d). When the droplet impacts the slag–manganese interface and is immersed in the molten manganese pool, sulfur in the droplet rapidly spreads out in the pool, and moreover, the sulfur concentration map is determined by the flow pattern of the molten manganese. From Figures 11(e) and (f), it is seen that the content of sulfur in the molten manganese at the center as well as the outer ring of the pool is lower. The main reason for this phenomenon is as follows: the molten manganese flows from the top outer ring to the top center of the pool, sinking to the bottom of the pool, and then flows back along the oblique solidification front as indicated in Figure 9. Sulfur is therefore converged at the top center of the pool, resulting in a higher sulfur concentration. Meanwhile, sulfur is taken away by the upward flow of the molten slag, just above the top center of the molten manganese pool. As a consequence, a larger concentration difference of sulfur is created. The desulfurization rate at the center of the slag–metal interface grows due to higher driving force of the chemical reaction. Besides, the vigorous motion of the molten manganese, caused by strong cooling, at the outer ring of the pool promotes the sulfur mass transfer at the outer edge of the slag–metal interface.

With freezing of the molten manganese, sulfur would enter it from the solidifying manganese, leading to a continual enrichment of sulfur at the solidification front. Additionally, sulfur in the molten manganese that is
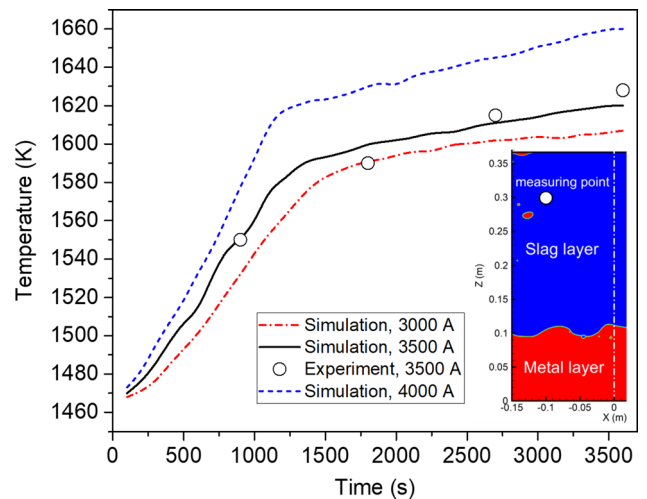

Fig. 12—Effect of applied current on slag temperature.

close to the solidification front get thoroughly mixed, since the solidification front moves upward slowly. The sulfur content in the solidified manganese would thus become more uniform. The re-distribution of sulfur within the solidified manganese becomes gradually hindered, so that only thermal diffusion of sulfur could be observed in the solid MM. The change of the concentration map, however, is negligibly small.

D. *Effect of Applied Current*

Figure 12 shows the effect of the applied current on the slag temperature, where the temperature measurement for the 3500 A applied current is also available. The slag temperatures al all three applied currents first rapidly rise, because the Joule heating is fast generated by the molten slag at the early stage. When the refining process reaches the steady state, the slag temperatures still slightly rise over time. It is crucial that the heat loss through the bottom of the mold is reduced, since the solidified manganese ingot gets higher and thus the vertical thermal resistance becomes larger.

The molten slag layer becomes hotter with the increasing applied current, as expected. The final temperature of the measuring point rises from 1607 K to 1660 K (1334 °C to 1387 °C) with the applied current ranging from 3000 to 4000 A. The rate of increase is approx. 0.8 pct when the applied current changes from 3000 to 3500 A, while the rate is about 2.5 pct if the applied current continuously rises to 4000 A. Higher temperatures strongly promote the diffusion, as well as the interfacial mass transfer of sulfur during the recycling process.

A comparative analysis of experimental and simulated slag temperatures at the applied current of 3500 A was also performed. It was found the most convenient to insert a thermocouple into the slag 60 mm below the free surface and between the water-cooled electrode and the inlet. The respective measurements were made in this point and compared to the calculated slag temperatures. A closer match between the measured and calculated
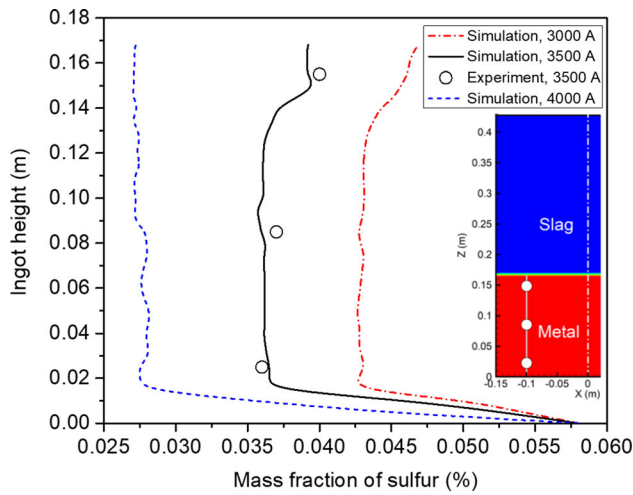
Fig. 13—Effect of applied current on sulfur concentration profile along vertical line in final manganese ingot.

Fig. 14—Effect of applied current on desulfurization rate.

data was obtained, and their deviation was within acceptable limits, which proves the developed model feasibility.

Figure 13 illustrates the sulfur concentration profiles along the vertical line in the final manganese ingot with all the three applied currents, where the sulfur concentration measurement of the ingot for the 3500 A applied current is also presented. A reasonable agreement between the experimental data and simulations was obtained. It can be seen that the sulfur content at the bottom of the ingot is quickly reduced. A 10 mm height of the molten MM with a 0.06 pct mass fraction sulfur was assumed at the beginning of the simulation, and sulfur at the upper layer of the initial molten MM was then removed. During the recycling process, sulfur in the molten manganese was continuously removed by the molten slag. The final amount of the residual sulfur in the MM was reduced with the increasing applied current. The calculated average sulfur content of the ingot dropped from 0.0447 to 0.0291 pct, when the applied current rose from 3000 to 4000 A. As mentioned above, larger applied currents would induce more Joule heating and higher Lorentz force in the melt, increasing the melt temperature and promoting the melt flow. The sulfur diffusion in the molten slag and molten manganese, as well as the interfacial mass transfer rate of sulfur, will be also notably enhanced. The desulfurization rate increases from 55.3 to 70.9 pct, as indicated in Figure 14.

At the final stage, the sulfur concentration exhibits a slight growth at the applied current values of 3000 and 3500 A (Figure 13). It appears that the sulfur concentration grows in the molten slag but drops in the molten manganese during the recycling process. As a result, the driving force for the desulfurization reaction is reduced, and the elimination of sulfur is delayed, especially at the final stage of the recycling process. The above driving force reduction may inhibit the desulfurization by offsetting at higher temperatures and melt flow promotion by the applied current increase to 4000 A. Given this, the removal rate remains unchanged.
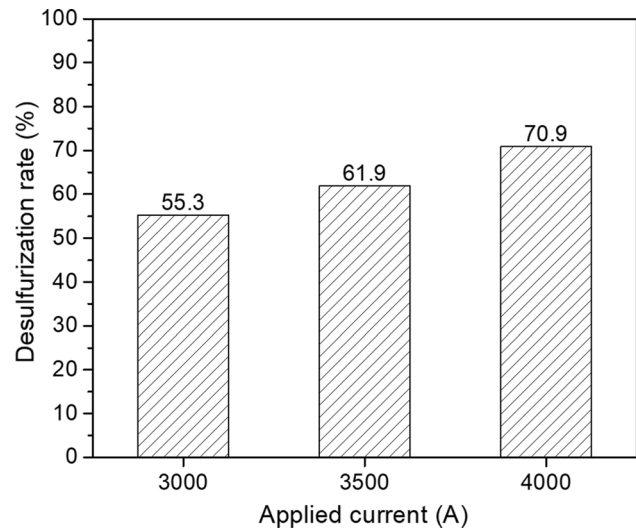
VI. CONCLUSIONS

An ESR furnace with a water-cooled electrode was innovatively used to refine the rejected EMM scrap for recycling. To clarify the desulfurization process in the rejected EMM scrap, a transient three-dimensional comprehensive numerical model was elaborated. Using the magnetic potential vector approach, the respective electromagnetic fields were calculated *via* the Maxwell equations. The Lorentz force and the Joule heating fields were derived as phase distribution functions and interrelated *via* the momentum and energy conservation equations as source terms, respectively. The molten MM droplet motion, as well as the fluctuation of the slag–metal interface, was described by the VOF approach. Besides, the solidification was modeled *via* the enthalpy-based technique. A thermodynamic module was established to estimate the sulfur mass transfer rate between the molten MM and the molten slag. Furthermore, a factor related to the magnitude and frequency of the alternating current and the physical properties of the melt was introduced to include the electro-emulsification phenomenon. An experiment has been carried out with a commercial-scale ESR device. The predicted values of the slag temperature and sulfur content in the final manganese ingot were found to agree reasonably with the corresponding measured data.

Under continuous melting of the rejected EMM scrap, molten MM droplets are formed at the domain inlet, grow, and fall down. Highly conductive molten MM droplets significantly change distributions of the current streamline, the Joule heating, and the Lorentz force around and within it. Moreover, droplets are inclined to rotate and move inside the mold. With the renewal of the slag–manganese interface, sulfur in the molten MM is constantly transferred to the molten slag. As for the molten manganese pool, the sulfur content at the center, as well as the outer ring of the pool, diminishes. The distribution of sulfur within the MM is gradually inhibited by the solidification process. With the applied current ranging from 3000 to 4000 A, the

average sulfur content of the manganese ingot dropped from 0.0447 to 0.0291 pct, and thus, the desulfurization rate rose from 55.3 to 70.9 pct.

REFERENCES

1. H. Karen: *J. Environ. Manag.*, 2009, vol. 90, pp. 3726–40.
2. N. Duan, Z.G. Dan, F. Wang, C.X. Pan, C.B. Zhou, and L.H. Jiang: *J. Clean Prod.*, 2011, vol. 19, pp. 2082–87.
3. J.M. Lu, D. Dreisinger, and T. Glück: *Hydrometallurgy*, 2014, vol. 141, pp. 105–16.
4. B.I. Medovar and G.A. Boyko: *Electroslag Technology*, Springer, New York, 1991, pp. 62–67.
5. V. Weber, A. Jardy, B. Dussoubs, D. Ablitzer, S. Rybéron, V. Schmitt, S. Hans, and H. Poisson: *Metall. Mater. Trans. B*, 2009, vol. 40B, pp. 271–80.
6. Q. Wang, Z. He, G.Q. Li, B.K. Li, C.Y. Zhu, and P.J. Chen: *Int. J. Heat Mass Transf.*, 2017, vol. 104, pp. 943–51.
7. S.M. Kang, D.Y. Kim, J.S. Kim, and H.G. Lee: *ISIJ Int.*, 2003, vol. 43, pp. 1683–90.
8. J. Lee and K. Morita: *ISIJ Int.*, 2004, vol. 44, pp. 235–42.
9. M.A. Rhamdhani, K.S. Coley, and G.A. Brooks: *Metall. Mater. Trans. B*, 2005, vol. 36B, pp. 591–604.
10. W.M. Cao, L. Muhmood, and S. Seetharaman: *Metall. Mater. Trans. B*, 2012, vol. 43B, pp. 363–69.
11. F.N.H. Schrama, E.M. Beunder, B. van den Berg, Y.X. Yang, and R. Boom: *Ironmak. Steelmak.*, 2017, vol. 44, pp. 333–43.
12. M. Alba, S.H. Jung, M.S. Kim, J.Y. Seol, S.J. Yi, and Y.B. Kang: *ISIJ Int.*, 2015, vol. 55, pp. 1581–90.
13. M. Kato, K. Hasegawa, S. Nomura, and M. Inouye: *Trans. ISIJ*, 1983, vol. 23, pp. 618–27.
14. D. Hou, Z.H. Jiang, Y.W. Dong, Y. Li, W. Dong, and F.B. Liu: *Metall. Mater. Trans. B*, 2017, vol. 48, pp. 1885–97.
15. Y. Liu, Z. Zhang, G.Q. Li, Q. Wang, L. Wang, and B.K. Li: *Steel Res. Int.*, 2017, vol. 88, p. 1700058.
16. M. Tao, B.S. Jin, W.Q. Zhong, Y.P. Yang, and R. Xiao: *Chem. Eng. J.*, 2010, vol. 159, pp. 149–58.
17. Q.G. Xiong, Y. Yang, F. Xu, Y.Y. Pan, J.C. Zhang, K. Hong, G. Lorenzini, and S.R. Wang: *ACS Sustain. Chem. Eng.*, 2017, vol. 5, pp. 2783–98.
18. Q. Wang, F. Wang, G.Q. Li, Y.M. Gao, and B.K. Li: *Int. J. Heat Mass Transf.*, 2017, vol. 113, pp. 1021–30.
19. A. Kharicha, E. Karimi-Sibaki, M. Wu, A. Ludwig, and J. Bohacek: *Steel Res. Int.*, 2018, vol. 89, p. 1700100.
20. J. Yanke, K. Fezi, R.W. Trice, and M.J.M. Krane: *Numer. Heat Transf. A*, 2015, vol. 67, pp. 268–92.
21. C.Y. Zhu, P.J. Chen, G.Q. Li, X.Y. Luo, and W. Zheng: *ISIJ Int.*, 2016, vol. 56, pp. 1368–77.
22. C.W. Hirt and B.D. Nichols: *J. Comput. Phys.*, 1981, vol. 39, pp. 201–25.
23. Z. Sun, P. Li, G.M. Lu, B. Li, J. Wang, and J.G. Yu: *Ind. Eng. Chem. Res.*, 2010, vol. 49, pp. 10798–10803.
24. J.U. Brackbill, D.B. Kothe, and C. Zemach: *J. Comput. Phys.*, 1992, vol. 100, pp. 335–54.
25. Q. Wang, R.J. Zhao, M. Fafard, and B.K. Li: *Appl. Therm. Eng.*, 2015, vol. 80, pp. 178–86.
26. A.H. Dilawari and J. Szekely: *Metall. Trans.*, 1977, vol. 8, pp. 227–36.
27. D. Krasnov, O. Zikanov, and T. Boeck: *Comput. Fluids*, 2011, vol. 50, pp. 46–59.
28. F. Felten, Y. Fautrelle, Y. Du Terrail, and O. Metais: *Appl. Math. Model.*, 2015, vol. 28, pp. 15–27.
29. Ansys Fluent Theory Guide, version 18.1; Ansys, Inc.: Canonsburg, PA, 2017.
30. C. Byon: *Int. J. Heat Mass Transf.*, 2014, vol. 88, pp. 20–27.
31. P.G. Jönsson and L.T.I. Jonsson: *ISIJ Int.*, 2001, vol. 41, pp. 1289–1302.
32. W.T. Lou and M.Y. Zhu: *Metall. Mater. Trans. B*, 2014, vol. 45B, pp. 1706–22.
33. T. Saitô and Y. Kawai: *Sci. Rep. Res. Inst. Tohoku Univ. Ser. A Phys. Chem. Metall.*, 1953, vol. 5, pp. 460–68.
34. Y. Kawai: *Sci. Rep. Res. Inst. Tohoku Univ. Ser. A Phys. Chem. Metall.*, 1957, vol. 9, pp. 78–83.
35. Y. Kawai: *Sci. Rep. Res. Inst. Tohoku Univ. Ser. A Phys. Chem. Metall.*, 1957, vol. 9, pp. 520–26.
36. S. Choi and A.V. Saveliev: *Phys. Rev. Fluids*, 2017, vol. 2, p. 063603.
37. H. Wang, Y.B. Zhong, Q. Li, Y.P. Fang, W.L. Ren, Z.S. Lei, and Z.M. Ren: *Metall. Mater. Trans. B*, 2017, vol. 48B, pp. 655–63.
38. O. Vizika and D.A. Saville: *J. Fluid Mech.*, 1992, vol. 239, pp. 1–21.
39. H.P. Yan, L.M. He, X.M. Luo, J. Wang, X. Huang, Y.L. Lü, and D.H. Yang: *Langmuir*, 2015, vol. 31, pp. 8275–83.
40. W. Duangkhamchan, F. Ronsse, F. Depypere, K. Dewettinck, and J.G. Pieters: *Chem. Eng. Sci.*, 2012, vol. 68, pp. 555–66.
41. X. Shi, Y. Xiang, L.X. Wen, and J.F. Chen: *Chem. Eng. J.*, 2013, vol. 228, pp. 1040–49.
42. Q. Wang, Z. He, B.K. Li, and F. Tsukihashi: *Metall. Mater. Trans. B*, 2014, vol. 45B, pp. 2425–41.
43. Q. Wang, L. Gosselin, and B.K. Li: *ISIJ Int.*, 2014, vol. 54, pp. 2821–30.